Multispectral Imaging of Continuum Emission for Determination of Temperature and Density Gradients Inside Implosion Plasmas

J. A. Koch, S. W. Haan, R. C. Mancini

U.S. Department of Energy

Lawrence
Livermore
National
Laboratory

March 17, 2003

DISCLAIMER

Multispectral Imaging of Continuum Emission for Determination of Temperature and Density Gradients Inside Implosion Plasmas

Jeffrey A. Koch[a,*], Steven W. Haan[a], Roberto C. Mancini[b]

[a]University of California, Lawrence Livermore National Laboratory
P.O. Box 808, L-481, Livermore CA, 94551

[b]Department of Physics, University of Nevada/Reno, Reno NV, 89557

Abstract

In inertial confinement fusion experiments, implosion of a cryogenic hydrogen isotope-filled capsule produces a plasma with a high-temperature, low-density core (the hot spot) surrounded by a low-temperature, high-density main fuel layer. Experimental measurements of temperature and density profiles in the hot spot are critical for implosion diagnosis. In this paper, we propose a simple technique for measuring core temperature and density profiles in cryogenic implosion plasmas. This technique uses absolutely calibrated continuum emission spectroscopy coupled with two-dimensional imaging to allow temperature and density profiles to be measured directly. We develop the technique analytically, and validate it using synthetic data and hydrodynamics simulation results. We find that the technique should be sufficiently accurate to measure central temperatures and densities to better than 20%. The technique may also find application to the diagnosis of other types of plasmas.

*Corresponding author.

E-mail address: koch1@llnl.gov

1. Introduction

The achievement of break-even and gain in inertial confinement fusion (ICF) experiments at the National Ignition Facility (NIF) and at other large facilities will rely on hot-spot ignition [1]. In this scheme, quasi-adiabatic compression of a spherical shell of cryogenic deuterium-tritium (DT) fuel results in a nearly isobaric compressed configuration, with a hot ($\sim$ 10 keV), low-density ($\sim$ 0.3 g/cm^2, 10 - 100 g/cm^3) hot spot surrounded by a cooler, high-density ($\sim$ 2 g/cm^2, $\sim$ 300 g/cm^3) main fuel layer (see Fig. 1). For ignition to occur, the central hot-spot must be hot enough to initiate thermonuclear reactions at a rate sufficient to overcome losses, and there must be sufficient areal density to keep alpha-particle fusion products from escaping. Achieving hot-spot parameters sufficient to ignite the main fuel is the chief technical challenge of ICF, and diagnosis of near-ignition ICF hot spots in NIF experiments is the primary motivation for this work.

Measurement of temperature and density within the central hot spot is therefore a critical diagnostic for the success of ICF. Measurement of temperature and density profiles near the central hot-spot could also provide information on poorly-understood conductive and turbulent-convective heat transfer processes which could reduce central temperatures and effective hot-spot areal densities. However, this measurement is complicated by the wide range of temperatures and densities near the central hot-spot, and by the presence of the colder, denser main fuel layer surrounding the hot-spot which contains most of the areal density of the compressed fuel. Absorption imaging is generally not feasible due to the need to create an x-ray backlight which produces sufficiently high x-ray energies to penetrate the dense main fuel layer and which is sufficiently bright to overcome self-emission from the hot spot. Additionally, spectroscopic tracers generally cannot be placed within

the cryogenic capsule because they would freeze out long before the DT forms an ice layer.

In order to address these issues, we have developed an experimental technique to measure temperature and density gradients within ICF implosion hot spots. This technique is based on absolutely-calibrated continuum emission x-ray spectroscopy coupled with two-dimensional x-ray imaging, and within the limitations of certain assumptions should allow quasi-three-dimensional reconstructions of the temperature and density profiles to be made. In the following sections, we will describe the technique in detail, and we will discuss error analyses we have performed using simulated data which demonstrate the potential and limitations of the technique.

2. Measurement Technique

The local power radiated via Bremsstrahlung by a fully-ionized plasma (per unit volume, per unit photon energy), at temperatures and photon energies much greater than Z^2 times the Rydberg energy, is given by [2, 3],

$$\varepsilon(E) = C \frac{Z^2 N_e N_i}{\sqrt{T}} \exp\left(\frac{-E}{T}\right) \bar{g}_{ff} \tag{1}$$

where C is a dimensional constant, N_e and N_i are the number densities of electrons and ions, T is the (single-temperature Maxwellian) plasma temperature in energy units, E is the Bremsstrahlung photon energy, and g_{ff} is the velocity-averaged free-free Gaunt factor which is a function of E and T, approximated for E > T as [2],

$$\bar{g}_{ff} \approx \sqrt{\frac{3T}{\pi E}} \qquad (2)$$

Using numerical values [2] for the dimensional constant C, for a hydrogen (Z=1) plasma we then have,

$$\varepsilon(E) = 1.50e - 32 \frac{N_e^2}{\sqrt{E}} \exp\left(\frac{-E}{T}\right) \qquad (3)$$

with $\varepsilon(E)$ in W cm^{-3} eV^{-1}, E and T in eV, and N_e in cm^{-3}. If we measure the local emissivity of the plasma at two different photon energies E_1 and $E_2 > E_1$ large enough that absorption can be neglected, then the emissivity ratio is simply related to temperature as,

$$\frac{\varepsilon(E_2)}{\varepsilon(E_1)} = \frac{\sqrt{E_1}}{\sqrt{E_2}} \exp\left(\frac{-(E_2 - E_1)}{T}\right) = \frac{\sqrt{E_1}}{\sqrt{E_2}} \exp\left(\frac{-\Delta E}{T}\right) \qquad (4)$$

This implies that the local temperature can be measured directly from the ratio of the local emissivities at E_1 and E_2,

$$T = \frac{\Delta E}{\ln\left(\frac{\sqrt{E_1}}{\sqrt{E_2}} \frac{\varepsilon(E_1)}{\varepsilon(E_2)}\right)} \qquad (5)$$

Given T from the emissivity ratios, we can infer the local density by back-substitution into Eq. (3), giving,

$$N_e = 8.16e + 15 * \varepsilon(E_1)^{1/2} E_1^{1/4} \exp\left(\frac{E_1}{2T}\right)$$
$$= 8.16e + 15 * \varepsilon(E_2)^{1/2} E_2^{1/4} \exp\left(\frac{E_2}{2T}\right)$$

(6)

Equations (5) and (6) are valid for any local point within the plasma, and at any particular time if the plasma parameters evolve in time. If we image the optically-thin plasma at energies E_1 and E_2 with an absolutely-calibrated instrument, we will obtain line-of-sight integrated emissivity (see Fig. 1). With assumptions of rotational symmetry about an axis perpendicular to the line of sight, we can perform Abel inversions [4] on the data to infer local emissivities as functions of local coordinates, such as radius in Fig. 1; eqs. (5) and (6) can then be used to infer temperature and density as functions of local position within the plasma. This is the essential concept behind the technique described in this paper, and while we used specific functional forms in eqs. (1) and (2), the concept is generally valid provided the final form of eq. (1) is simple enough that the two equations, for emissivity at two energies, can be solved for the two variables of temperature and density.

There are several experimental approaches which could be used to obtain the multispectral imaging data required for the application of our measurement technique. The first and simplest, shown schematically in Fig. 1, is a multiple-pinhole x-ray spectrometer [5]. This instrument records multiple x-ray images which are spectrally isolated due to reflection off a Bragg mirror placed behind the pinhole array. The spectral content of each image is then determined by the spectral bandpass of the mirror and by the geometry of the instrument. This type of instrument has already been utilized for implosion multispectral imaging [6, 7], and the main additional constraint imposed by the present application is the need to absolutely

calibrate the image intensity. Additionally, careful corrections for effects such as fluorescence from the instrument housing will be necessary, using information from different parts of the image plane to quantify different sources of x-ray emission [8].

If pinhole projection cannot be utilized for any reason, then x-ray optics could be used instead. One approach is to use multiple two-dimensional imaging crystals, each of which is tuned to a different photon energy; a second approach is to use multiple Kirkpatrick-Baez microscopes, with each tuned to reflect a different photon energy. Both approaches have been used for multispectral imaging of implosion plasmas [9, 10], though the required absolute calibrations would be difficult and would have to be applied to each imaging channel separately.

The principal experimental requirement is the ability to obtain quasi-monochromatic x-ray images in different energy bands, with an absolutely calibrated instrument that allows image brightness to be related to source brightness in absolute units. The x-ray bands must be sufficiently high in energy to make reabsorption by the colder, denser main fuel layer negligible, and should be chosen to provide substantially different emissivities which are nearly inversely proportional to temperature. The solution to the latter consideration can be estimated analytically from eq. (1). Neglecting g_{ff}, assuming $\varepsilon \propto \exp(-E/T)/\sqrt{T}$, and taking derivatives with respect to T and E, we find,

$$\frac{|d\varepsilon|}{\varepsilon} = \frac{\Delta E}{T} \tag{7}$$

$$\frac{|d\varepsilon|}{\varepsilon} = \frac{dT}{T}\left(\frac{E}{T} - \frac{1}{2}\right) \tag{8}$$

This implies that we should image at photon energies $E > 3T/2$ for a fractional change in emissivity greater than a fractional change in temperature, and that we should use $\Delta E > T/2$ to obtain greater than a factor-of-2 change in emissivity at fixed temperature. The actual operating photon energies must take absorption by the main fuel into account.

Since the plasma parameters are in fact time-varying, the x-ray images must be time-gated temporal snapshots, or must be referenced to time-gated images or streaked spectra which can be used to unfold the time history of the temperature and density profiles. The Abel inversion procedure additionally places symmetry requirements upon the plasma that must be met. We examine these issues in the following sections.

3. Analysis of Simulated Time-Gated Data

In order to assess the quantitative accuracy of our hot-spot diagnostic, we analyzed synthetic x-ray imaging data derived from two sources. First, we created temperature, density and emissivity profiles for which the Abel inversion procedure can be performed analytically, and we used the profiles to generate synthetic x-ray images. These images were used to test the numerical Abel inversion procedures we used, and to investigate the required specifications on the calibrations of the instrumentation. Second, we performed one-dimensional hydrodynamics simulations of a capsule implosion using the code Hydra [11], and generated synthetic x-ray images which were used to test the overall accuracy of the temperature and density profile reconstruction. In this Section, both types of synthetic data are treated as temporal snapshots, and no time variations in the temperature and density profiles are considered.

We first arbitrarily assume a spherically-symmetric plasma with two-dimensional image profiles given by,

$$I(x; E = 3500eV) = 2K \exp\left(\frac{-x^2}{(50\mu m)^2}\right)$$

$$I(x; E = 4500eV) = K \exp\left(\frac{-x^2}{(45\mu m)^2}\right)$$

(9)

where I(x) is the line-of-sight integrated image brightness along the projected equator and K is an (arbitrary) dimensional constant. The photon energies and other parameters were chosen in anticipation of the implosion simulation results discussed later. The Abel transforms between radial emissivity and line-integrated two-dimensional image brightness are [4],

$$\varepsilon(r) = \frac{-1}{\pi} \int_r^R dx \frac{(dI(x)/dx)}{\sqrt{x^2 - r^2}}$$

(10)

$$I(x) = 2 \int_x^R \frac{r\varepsilon(r)}{\sqrt{r^2 - x^2}} dr$$

(11)

where R is the maximum radius of the spherical emitter. Implicit in these transforms are the assumptions that $\varepsilon(r)$ falls to zero at r = R, and that $d\varepsilon/dr = 0$ at r = 0. Here, we assume spherical symmetry and r is the spherical-coordinate radius, but the Abel transforms could also be used for cylindrically-symmetric plasmas, in which case r is the cylindrical-coordinate radius and the image profiles are referenced to a specific z-coordinate. With I(x) given by eqs. (9), we find that,

$$\varepsilon(r; E = 3500eV) = \frac{2K}{(50\mu m)\sqrt{\pi}} \exp\left(\frac{-r^2}{(50\mu m)^2}\right)$$

$$\varepsilon(r; E = 4500eV) = \frac{K}{(45\mu m)\sqrt{\pi}} \exp\left(\frac{-r^2}{(45\mu m)^2}\right) \tag{12}$$

Using eqs. (5) and (6), we find that T(r) and N(r) are given by,

$$T(r) = \frac{1000eV}{0.462 + \frac{r^2}{(103.2\mu m)^2}} \tag{13}$$

$$N(r) = 2.118e + 16 * \sqrt{K} \exp\left(\frac{-r^2}{(167.1\mu m)^2}\right) \tag{14}$$

With these analytical results, we can create synthetic image intensity profiles using eqs. (9) and analyze them numerically as if they were real experimental data in order to check that eqs. (13) and (14) are correctly reproduced. For this process, we use a numerical implementation of the Abel transforms [4] and eqs. (5) and (6). The results of this analysis are shown in Fig. 2. We find that, given data of sufficient quality , we can extract T(r) and N(r) to high precision.

If we rewrite eqs. (9) as,

$$I(x; E = 3500eV) = 2\alpha K \exp\left(\frac{-x^2}{(50\mu m)^2}\right)$$

$$I(x; E = 4500eV) = K \exp\left(\frac{-x^2}{(45\mu m)^2}\right) \tag{15}$$

and write E_1 and E_2 as,

$$E_1 = 3500\beta$$
$$E_2 = E_1 + \Delta E = 3500\beta + 1000\gamma \tag{16}$$

then we can write T(r) and N(r) as,

$$T(r) = \frac{1000\gamma}{\ln\left(\dfrac{1.8\alpha}{\sqrt{1+\dfrac{\gamma}{3.5\beta}}}\right) + \dfrac{r^2}{(103.2\mu m)^2}} \tag{17}$$

$$N(r) = 9.432e+15 * \sqrt{K\alpha\sqrt{\beta}}\left(\dfrac{1.8\alpha}{\sqrt{1+\dfrac{\gamma}{3.5\beta}}}\right)^{\frac{1.75\beta}{\gamma}} \exp\left(\dfrac{-r^2}{(70.7\mu m)^2}\left(1-0.82\dfrac{\beta}{\gamma}\right)\right) \tag{18}$$

Eqs. (17) and (18) are useful because they allow the constants K, α, β and γ to be varied from unity in order to find the corresponding variations in T(r=0) and N(r=0). Assuming the errors are independent and add in quadrature, we find that achieving precisions of 20% in measured central temperatures and densities requires measurement precisions as shown in Table 1. These measurement precisions appear to be challenging but reasonable, and we conclude that a hot-spot temperature and density diagnostic based on continuum imaging spectroscopy is feasible and can provide central values accurate to better than 20% provided all systematic errors are understood and accounted for. The accuracy of the process for temperatures and densities at r > 0 is more difficult to assess, and will probably depend more sensitively on the signal to noise ratio of the experimental data.

We next used the hydrodynamics code Hydra [11] to simulate the direct-drive implosion of a cryogenic deuterium capsule, using parameters typical of those achieved in current experiments at the Omega Laser Facility [12]. This simulation is one-dimensional and does not include asymmetries due to beam energy and pointing imbalances, target imperfections, and other effects, but does include thermal conduction and radiation transport effects. The simulated capsule was 914 mm in diameter, with a 2 μm-thick plastic shell surrounding a 90 μm-thick layer of deuterium ice with a central void containing deuterium gas at a density of 0.48 mg/cm^3; the implosion drive was 28 kJ in a 1 ns-square temporal pulse shape. Simulated x-ray image profiles at 3.5 and 4.5 keV photon energies, with perfect and 10 μm spatial resolution, are shown in Fig. 3, while simulated temperature and density profiles as functions of radius are shown in Fig. 4. The simulated x-ray images were obtained from radiation transfer, and include both local emission and absorption from the deuterium plasma and from the hydrocarbon plasma created from the remains of the plastic shell. The photon energies 3.5 and 4.5 keV were chosen to provide approximately a factor-of-2 change in image brightness (from eq. (7)) while avoiding significant reabsorption from the main-fuel hydrogen or the outer hydrocarbon plasma.

We then Abel-inverted the simulated x-ray images to obtain ε(r, E=3500 eV) and ε(r, E=4500 eV). Hydra uses a Bremsstrahlung emissivity model that is more complex than eq. (3), but can be approximated in this regime by:

$$\varepsilon_{Hydra}(E) = 2.2e - 32 * \frac{N_e^2}{T^{0.2}E^{0.4}} \exp\left(\frac{-E}{T}\right) \tag{19}$$

Equations (5) and (6) then become:

$$T = \frac{\Delta E}{\ln\left(\frac{\varepsilon(E_1)}{\varepsilon(E_2)}\left(\frac{E_1}{E_2}\right)^{0.4}\right)} \qquad (20)$$

$$N_e = 6.7e+15 * \varepsilon(E_1)^{1/2} E_1^{0.2} T^{0.1} \exp\left(\frac{E_1}{2T}\right) \qquad (21)$$

The results of our analysis of the simulated Hydra x-ray images, using eqs. (20) and (21) to relate temperature and density profiles to emissivity profiles, are overlaid in Fig. 4. We find that in this case, our technique recovers both T(r=0) and ρ(r=0) to better than 1.5% when image spatial resolution is perfect. When 10 μm spatial smoothing is added to the images profiles, our technique recovers T(r=0) to better than 4.5% and recovers ρ(r=0) essentially perfectly, with both inferred profiles becoming less accurate at larger radii where gradients become more steep.

4. Analysis of Synthetic Time-Integrated Data

The analysis discussed so far has implicitly assumed that either the plasma parameters do not vary in time, or that the image data is gated over a time interval short compared with the timescale for plasma parameter evolution. Generally, this will not be true, because the plasma parameters change over ~ 50 ps timescales and because gated image data will be very difficult and probably impossible to calibrate to the precisions listed in Table 1. Image data with the required calibration precision will likely need to be time-integrated, and corrections and additional information will therefore be required. The reason for the requirement for additional information can be seen analytically, because if the temperature and density profiles vary in time,

the image intensity profiles (from eq. (11)) will also vary in time. Using eq. (3) for the local emissivity, we find,

$$I(x,t;E) \propto \frac{1}{\sqrt{E}} \int_x^R \frac{r}{\sqrt{r^2 - x^2}} N_e^2(r,t) \exp\left(\frac{-E}{T(r,t)}\right) dr \qquad (22)$$

The time-integrated image intensity profile is then,

$$\bar{I}(x;E) \propto \frac{1}{\sqrt{E}} \int_{-\infty}^{\infty} dt \int_x^R dr \frac{r}{\sqrt{r^2 - x^2}} N_e^2(r,t) \exp\left(\frac{-E}{T(r,t)}\right) \qquad (23)$$

The dual-integral precludes the use of the conventional Abel inversion formula eq. (10).

The simplest approach to unfolding time-evolution effects is to couple absolutely-calibrated time-integrated multispectral imaging data with relatively-calibrated, time-gated multispectral imaging data. Relative calibration of gated data will be simpler than absolute calibration, and as long as a sufficient number of gated frames can be obtained to cover the temporal evolution of the emissivity, then the absolutely-calibrated, time-integrated data can be used to normalize the intensity of the gated data.

If gated imaging data of sufficient quality can not be simultaneously obtained, then an alternative approach to recovering peak temperature and density profiles at the time of peak emission from time-integrated image data is to couple it to time-resolved, spatially-integrated spectra. We can write the spectrum as,

$$\bar{J}(t;E) \propto \frac{1}{\sqrt{E}} \int_0^R dx \int_x^R dr \frac{xr}{\sqrt{r^2 - x^2}} N_e^2(r,t) \exp\left(\frac{-E}{T(r,t)}\right) \qquad (24)$$

If we make a simplifying assumption that T(r,t) does not change significantly in time over the period when the density is highest, and if we assume that N(r,t) is a separable function N(r,t) = f(t)*g(r), then we can write

$$\bar{J}(t;E) \propto \frac{1}{\sqrt{E}} f^2(t) \int_0^R dx \int_x^R dr \frac{xr}{\sqrt{r^2 - x^2}} g^2(r) \exp\left(\frac{-E}{T(r)}\right) \tag{25}$$

$$\bar{I}(x;E) \propto \frac{1}{\sqrt{E}} \int_{-\infty}^{\infty} dt f^2(t) \int_x^R dr \frac{r}{\sqrt{r^2 - x^2}} g^2(r) \exp\left(\frac{-E}{T(r)}\right) = I(x,t;E) * \int_{-\infty}^{\infty} \frac{\bar{J}(t;E)}{\bar{J}(t=0;E)} dt \tag{26}$$

Therefore, a first approximation to the peak (in time) temperature and density profiles can be obtained by using the time-integrated image intensity profiles after first dividing them by the time-integral of the space-integrated time-resolved spectrum, which is normalized to unity at the time of peak emissivity.

Figure 5 shows the temporal history of central (r = 0) temperature and density from the Hydra simulation described in Section 3, along with the simulated space-integrated time-resolved image intensity at 3.5 and 4.5 keV. Integrating the time profiles and dividing the image intensity profiles shown in Fig. 3 by these integrals, we obtain the temperature and density profiles shown in Fig. 6. We find that in this case, our technique recovers both T(r=0, t=peak) and ρ(r=0, t=peak) to better than 14.5% when the image resolution is perfect. When the images are smoothed with 10 μm spatial resolution, our technique recovers T(r=0, t=peak) to within 16% and recovers ρ(r=0, t=peak) to within 19%.

Since the assumptions required above (that T(r,t) does not change significantly in time over the period when the density is highest, and that

N(r,t) is a separable function) are not generally true, the only recourse to obtaining better results from time-integrated image data when corresponding relatively-calibrated gated image data is unavailable is to use a multi-objective data analysis in order to find solutions to T(r,t) and N(r,t) which simultaneously satisfy eqs. (23) and (24). In this case, we search in a parameter space for T(r,t) and N(r,t) subject to the conditions of simultaneously yielding best fits (e.g. in a least-square minimization sense) to the absolutely-calibrated, time-integrated image intensity profiles and to the spatially-integrated, time-resolved spectra. Multi-objective data analysis using genetic algorithms has been successfully applied to the determination of implosion core gradients based on the self-consistent and simultaneous analysis of x-ray line monochromatic images and space-integrated x-ray line spectra from Ar-doped implosions [7, 13, 14]. Here, multi-objective data analysis could provide better results for N(r=0, t=peak) and T(r=0, t=peak) than were obtained analytically, and could reduce systematic errors below the levels estimated above. Preliminary tests of the application of multi-objective data analysis to this problem based on the use of a niched-Pareto genetic algorithm are encouraging, and we will investigate this approach to unfolding temporal variations in temperature and density in a future paper.

5. Summary and Conclusions

We have described a novel technique for measuring temperature and density profiles in ICF implosion hot spots. The technique uses multiple quasi-monochromatic continuum emission x-ray images obtained at different photon energies which are sufficiently high that the temperature sensitivity of the x-ray emissivity is high and that the absorption by the surrounding plasma is negligible. Abel-inverting the image profiles allows the emissivity

profiles to be extracted, and manipulation of the emissivity profiles allows the temperature and density profiles to be derived separately. We have described several approaches to experimentally obtaining these multispectral x-ray image data, each of which has already been applied to previous ICF experiments.

We have investigated how calibration errors limit the precision of the technique, and have found that 20% measurement precision of the central temperature and density appears feasible. We have also performed hydrodynamics simulations of Omega implosions and analyzed the synthetic image data, and have found good agreement with the (known) central temperatures and densities when temporal evolution is neglected, with systematic errors of less than 1.5% in central T and ρ; the errors increase to 4.5% in central T and decrease to essentially zero in central ρ when 10 μm image resolution limitations are included. The addition of temporal variations in temperature and density contribute to systematic errors that are on the order of 14.5% in central T and ρ for perfect image spatial resolution, and 16% in central T and 19% in central ρ for 10 μm image spatial resolution, when a simple analytical approximation for the temporal evolution is used. We have also discussed several alternative approaches which might be used to allow time-evolution errors to be reduced. We suggest that the technique will be valuable for cryogenic implosion plasma diagnosis, and potentially critical for the success of ICF ignition experiments at the NIF.

Because of the requirement that absorption and emission by higher-Z plasma surrounding the hot spot is negligible, our technique is likely restricted to the implosion of cryogenic capsules, where the pusher layer is a low atomic number material such as deuterium and tritium and where the outer shell is transparent to the core x-rays. However, we envision that three-

dimensional temperature and density profiles might be obtained through the use of multiple line-of-sight views. In this case, the symmetry requirements are relaxed, and the reconstruction technique should allow the application of quantitative multispectral continuum imaging to implosions that are far from ideally spherically or cylindrically symmetric. Finally, we note that the technique described here is generally applicable to any bremsstrahlung-emitting body that has sufficient symmetry to allow the Abel inversion to be performed, and that is essentially transparent to the radiation being observed.

References

[1] Lindl JD. Inertial Confinement Fusion. New York: AIP Press/Springer-Verlag, 1998.

[2] Rybicki GB, Lightman AP. Radiative Processes in Astrophysics. New York: John Wiley and Sons, 1979.

[3] Griem HR. Principles of Plasma Spectroscopy. Cambridge: Cambridge University Press, 1997.

[4] Bockasten K. J. Opt. Soc. Am. 1961: 51, 943.

[5] Yaakobi B, Marshall FJ, Bradley DK. Applied Optics 1998: 37, 8074.

[6] Yaakobi B, Smalyuk VA, Delettrez JA, Marshall FJ, Meyerhofer DD, Seka W. Phys. Plasmas 2000: 7, 3727.

[7] Welser LA, Mancini RC, Koch JA, Izumi N, Dalhed H, Scott H, Barbee TW, Jr., Lee RW, Golovkin IE, Marshall F, Delettrez J, Klein L. J. Quant. Spectrosc. Radiat. Transfer (in press).

[8] Perry TS, Davidson SJ, Serduke FJ, Bach DR, Smith CC, Foster JM, Doyas RJ, Ward RA, Iglesias CA, Rogers FJ, Abdallah J, Jr., Stewart RE, Kilkenny JD, Lee RW. Phys. Rev. Lett. 1991: 67, 3784.

[9] I. Uschmann I, Fujita K, Niki I, Butzbach R, Nishimura H, Funakura J, Nakai M, Forster E, Mima K. Applied Optics 2000: 39, 5865.

[10] Smalyuk VA, Dumanis SB, Marshall FJ, Delettrez JA, Meyerhofer DD, Regan SP, Sangster TC, Yaakobi B, Koch JA. Physics of Plasmas (in press).

[11] Marinak MM, Tipton RE, Landen OL, Murphy TJ, Amendt P, Haan SW, Hatchett SP, Keane CJ, McEachern R, Wallace R. Phys. Plasmas 1996: 3, 2070.

[12] Stoeckl C, Chiritescu C, Delettrez JA, Epstein R, Glebov VY, Harding DR, Keck RL, Loucks SJ, Lund L, McCrory RL, McKenty PW, Marshall FJ, Meyerhofer DD, Morse SF, Regan SP, Radha PB, Roberts S, Sangster TC,

Seka, Skupsky S, Smalyuk VA, Sorce C, Soures JM, Town RP, Frenje JA, Li CK, Petrasso RD, Seguin FH, Fletcher K, Paladino S, Freeman C, Izumi N, Lerche R, Phillips TW. Phys. Plasmas 2002: 9, 2195.

[13] Golovkin I, Mancini R, Louis S, Ochi Y, Fujita K, Nishimura H, Shirga H, Miyanaga N, Azechi H, Butzbach R, Uschmann I, Foerster E, Delettrez J, Koch J, Lee RW, Klein L. Phys. Rev. Letters 2002: 88, 045002-1.

[14] Golovkin IE, Mancini RC, Louis S, Lee RW, Klein L. J. Quant. Spectrosc. Radiat. Transfer 2002: 75, 625.

Figure Captions

Figure 1: Schematic of one possible implementation of multispectral x-ray imaging for determination of core temperature and density gradients. In this example, multiple monochromatic images are obtained from a multiple pinhole array coupled to a Bragg mirror. Each image is a monochromatic line-of-sight integral map of the plasma emissivity.

Figure 2: Temperature and density profiles inferred from Abel-inversion of x-ray image intensity profiles, compared with input temperature and density profiles used to calculate the x-ray image intensity profiles, using equations (9) - (14).

Figure 3: Simulated x-ray image intensity profiles from the Hydra hydrodynamic simulations discussed in Section 3. The unsmoothed curves are for perfect spatial resolution.

Figure 4: Temperature and density profiles inferred from Abel-inversion of x-ray image intensity profiles from Fig. 3, compared with actual temperature and density profiles from the Hydra simulations. The 0 μm cases use the unsmoothed curves from Fig. 3.

Figure 5: Temporal variations in central T_e, central ρ, and spatially-integrated 3.5 keV and 4.5 keV x-ray emission from the Hydra simulations.

Figure 6: Peak (in time) temperature and density profiles inferred from Abel-inversion of time-integrated x-ray image intensity profiles (using eq. (26)), compared with actual peak (in time) temperature and density profiles, from the Hydra simulations described in Section 3. The 0 μm cases use the unsmoothed curves from Fig. 3.
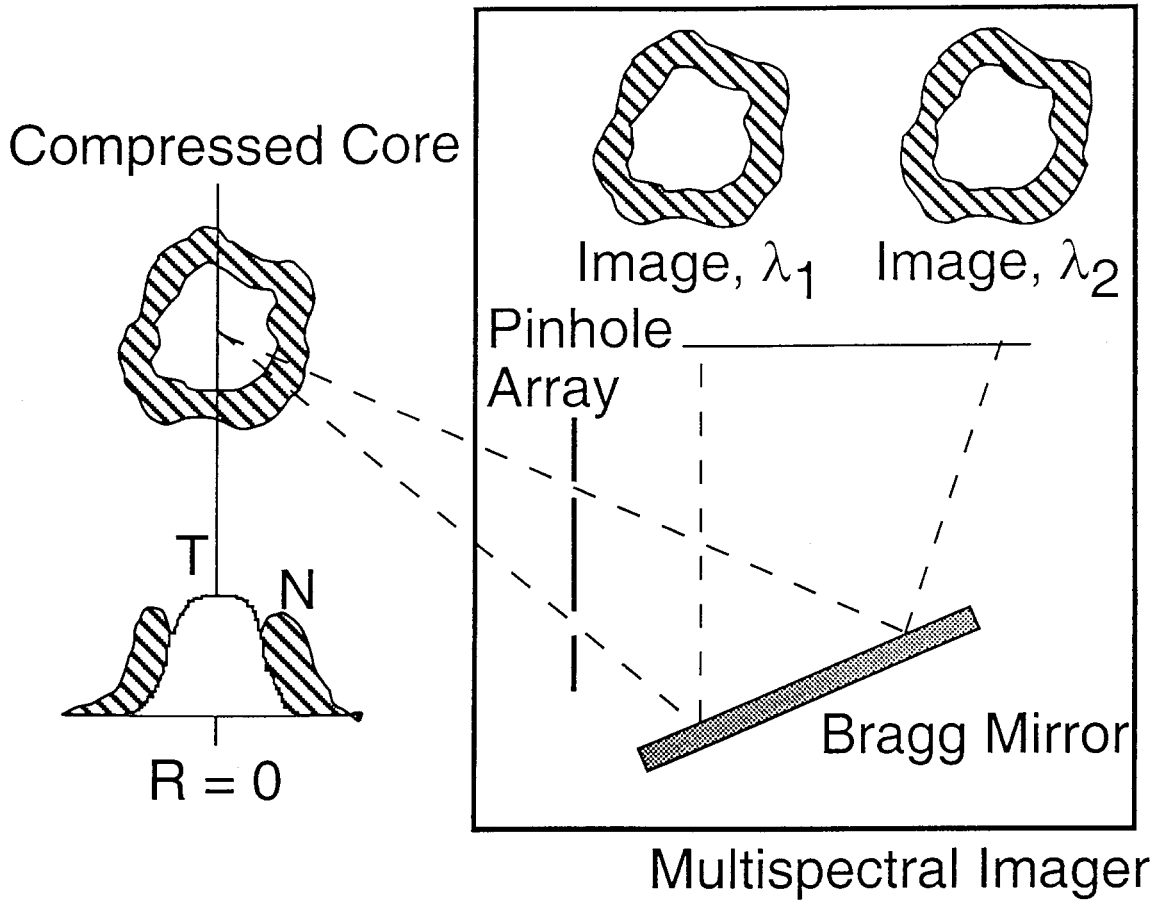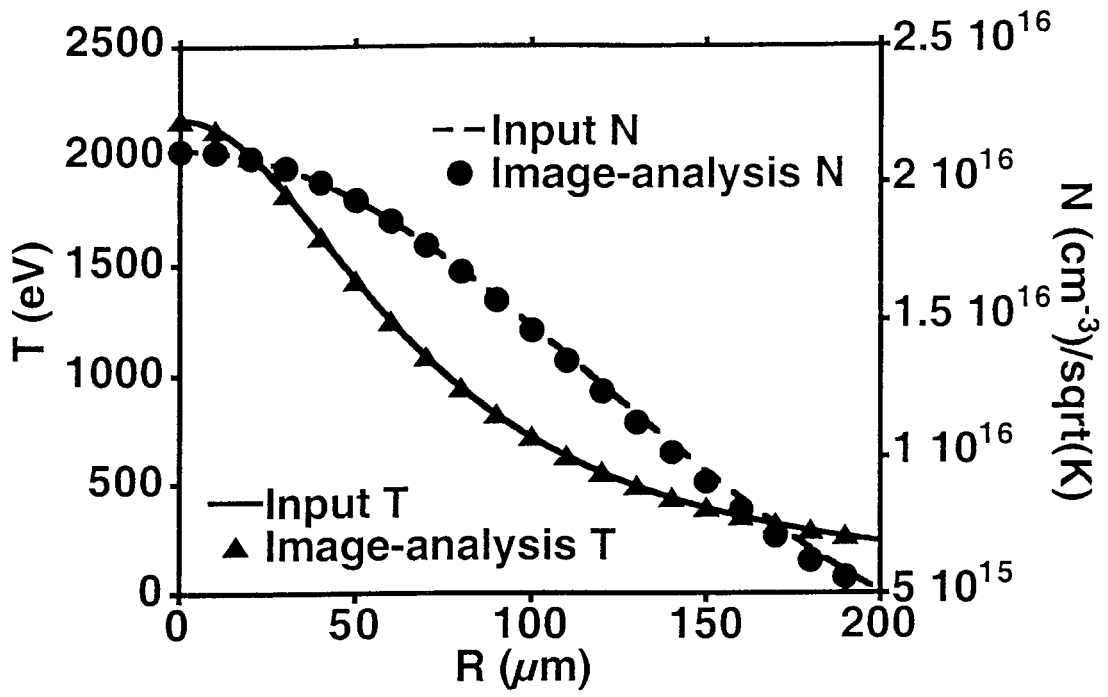
Figure 1

Figure 2

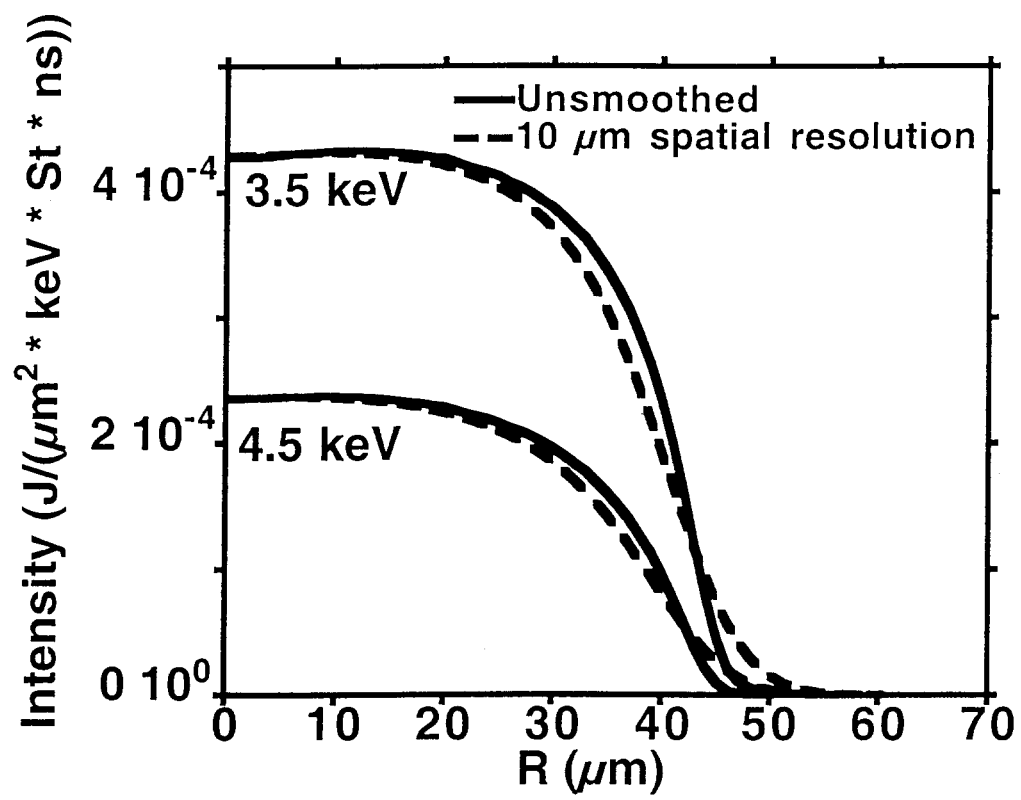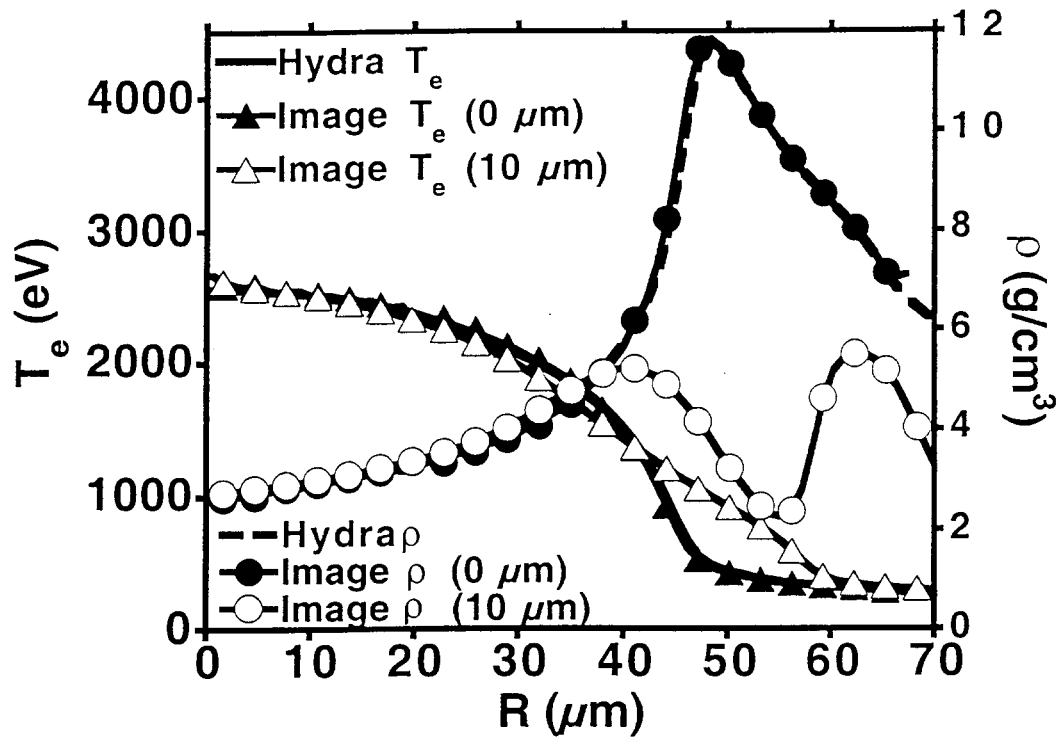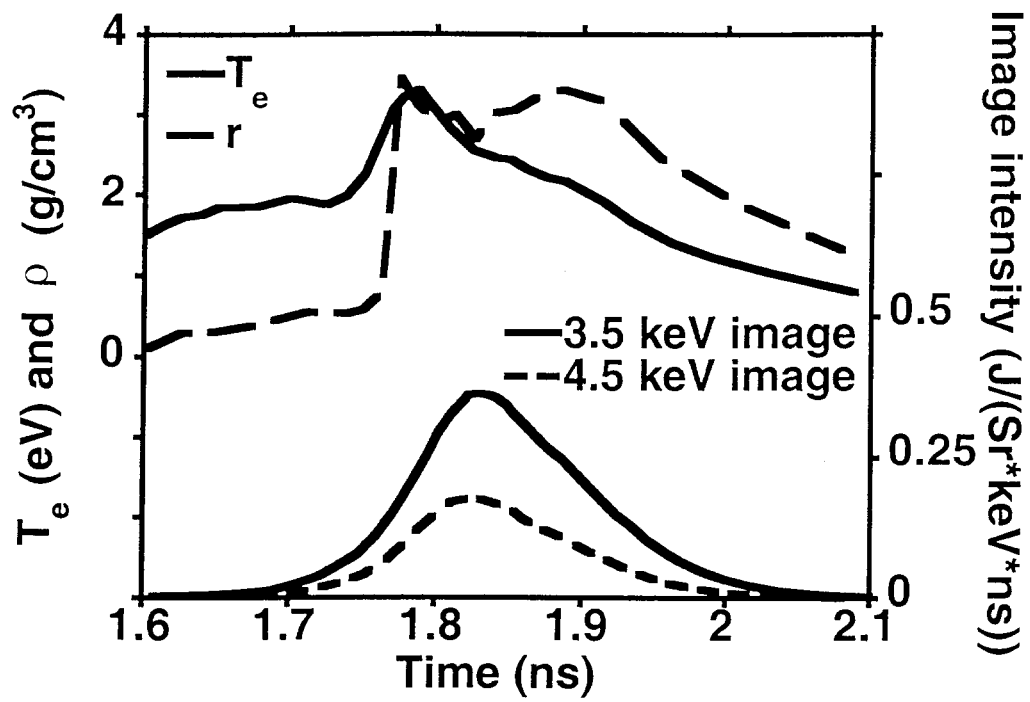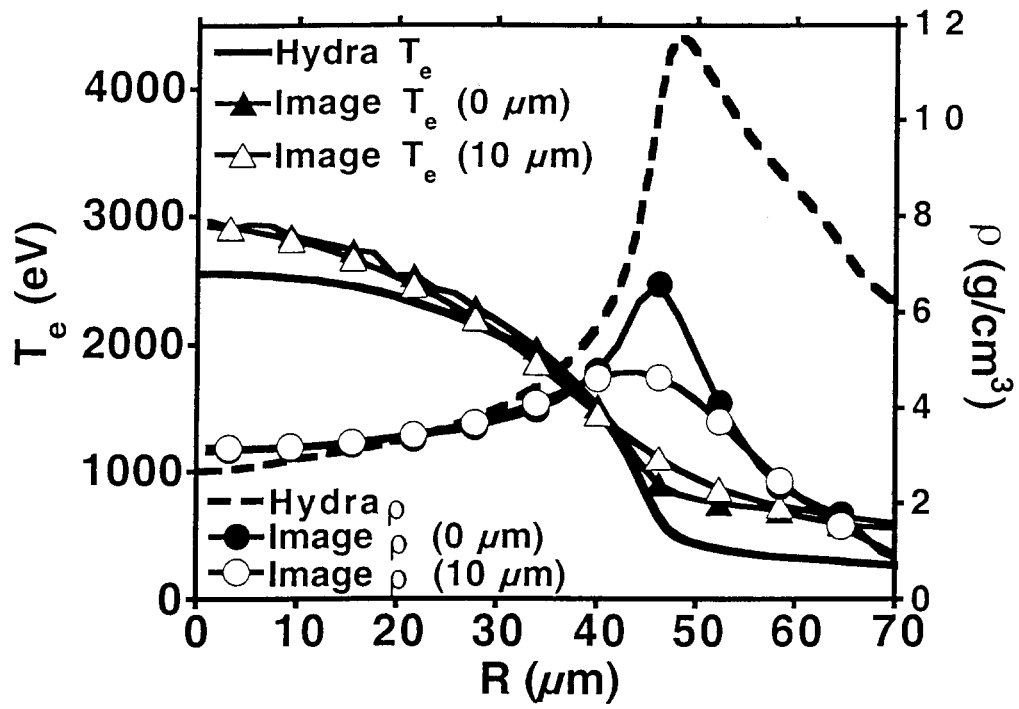Figure 3

Figure 4

Figure 5

Figure 6

Table 1: Estimated Measurement Precisions Required for Measurement of T(r=0) and N(r=0) to 20%

Quantity	For 20% precision in T(r=0)	For 20% precision in N(r=0)
Absolute intensity calibration	not applicable	20%
Relative intensity calibration	7%	5%
Energy scale reference	coarse	8%
Energy scale dispersion	11%	10%

Uncertainty in T(r=0) assumes that two errors add in quadrature, while uncertainty in N(r=0) assumes four errors add in quadrature. Only coarse (~ 50%) precision in the energy scale reference point is required for precise measurements of T(r=0).